

Banner appropriate to article type will appear here in typeset article

Passive cell body plays active roles in microalgal swimming via nonreciprocal interactions

Xiaoping Hu¹, Zhaorong Liu², Da Wei³ and Shiyuan Hu^{1†}

¹School of Physics, Beihang University, Beijing 100191, China

²Department of Physics, University of Science and Technology of China, Hefei, Anhui 230026, China

³Beijing National Laboratory for Condensed Matter Physics, Institute of Physics, Chinese Academy of Sciences, Beijing 100190, China

(Received xx; revised xx; accepted xx)

The cell body of flagellated microalgae is commonly considered to act merely as a passive load during swimming, and a larger body size would simply reduce the speed. In this work, we use numerical simulations based on a boundary element method to investigate the effect of body-flagella hydrodynamic interactions (HIs) on the swimming performance of the biflagellate, *C. reinhardtii*. We find that body-flagella HIs significantly enhance the swimming speed and efficiency. As the body size increases, the competition between the enhanced HIs and the increased viscous drag leads to an optimal body size for swimming. Based on the simplified three-sphere model, we further demonstrate that the enhancement by body-flagella HIs arises from an effective nonreciprocity: the body affects the flagella more strongly during the power stroke, while the flagella affect the body more strongly during the recovery stroke. Our results have implications for both microalgal swimming and laboratory designs of biohybrid microrobots.

Key words:

1. Introduction

The unicellular green alga *C. reinhardtii* has been widely used as a model organism for studying various problems in fluid dynamics and cell biology (Goldstein 2015), such as tactic behaviors (Leptos *et al.* 2023), flagellar dynamics (Quaranta *et al.* 2015; Sartori *et al.* 2016), and single cell flow fields (Drescher *et al.* 2010; Wei *et al.* 2019, 2021). The wild-type cell of *C. reinhardtii* has two flagella anchored at the anterior side of the spheroidal cell body. During swimming, the two flagella beat approximately in a two-dimensional plane, with a breaststroke-like gait consisting of distinct power and recovery strokes. It is now well established that flagellar beating is driven by distributed molecular motors, a characteristic conserved across eukaryotic cells. Studies of the swimming mechanisms of green algae have

† Email address for correspondence: shiyuanhu@buaa.edu.cn

inspired numerous designs of artificial flagella and microswimmers (see e.g., Diaz *et al.* 2021; Moreau *et al.* 2024).

The modeling of eukaryotic flagellar dynamics dates back to Machin (1958), in which the bending waves of an elastic beam actuated at the boundary are solved. Although this boundary-driven model is a significant simplification of realistic flagellar dynamics, later developments reveal the effects of various physical elements on flagellar propulsion, such as flexibility (Wiggins & Goldstein 1998; Peng *et al.* 2017), swimmer geometry (Lauga 2007), flagellar curvature (Liu *et al.* 2020; Hu *et al.* 2022), and hydrodynamic interactions (Elfasi *et al.* 2018; Hu & Meng 2024). On the other hand, studies that combine mechanical models of flagellar deformation with molecular motor dynamics focus on how beating waveforms are regulated (see review Gilpin *et al.* 2020).

In most previous studies, the flagellar base is assumed to be fixed in place. Combining flagellar beating with a moving cell body has received much less attention, and yet it is crucial for understanding the swimming mechanisms. In addition to mechanical coupling at the flagellar base, the cell body and flagella are also coupled through complex hydrodynamic interactions (HIs). Over a beating period, the cell body moves back and forth, entraining a considerable volume of fluid. At low Reynolds number (Re), this body-induced flow decays slowly in space and can significantly influence flagellar propulsion. Meanwhile, the flow induced by the flagella also modifies the drag force acting on the cell body. As a minimal swimming model, the three-sphere model, in which the flagellar beating is represented by spheres moving along closed orbits, provides insights into flagellar synchronization (Friedrich & Jülicher 2012), run-and-tumble behavior (Bennett & Golestanian 2013), and three-dimensional helical trajectories (Cortese & Wan 2021). Optimal gaits for swimming and feeding have been identified using numerical optimization (Tam & Hosoi 2011), where the swimming dynamics is modeled via flow singularities placed along the flagella and at the center of the cell body. Although these studies reveal different dynamic behaviors of microalgal swimming, the effect of body-flagella HIs on swimming performance remains elusive. In recent work (Hu & Meng 2024), we modeled the swimming dynamics of multiflagellated microalgae and demonstrated that body-flagella HIs determine the hydrodynamic advantage of multiflagellarity. In particular, swimming efficiency increases monotonically with the number of flagella only when they are attached to the anterior side of the cell body. However, whether an optimal body size exists for microalgal swimming is still an open question.

In this work, we use numerical simulations to investigate the effect of body-flagella HIs on the swimming performance of *C. reinhardtii*. We prescribe the flagellar waveform based on experimental measurements and incorporate both body-flagella and interflagellar HIs using a boundary element method. We find that body-flagella HIs can significantly enhance the swimming performance and lead to an optimal body size for both speed and efficiency. Further analysis based on the three-sphere model reveals that body-flagella HIs are effectively nonreciprocal.

2. Simulation model

Our swimming model of *C. reinhardtii* consists of two flagella of length L and a spheroidal cell body with semi-minor axis a and semi-major axis b . The flagellar waveform of a *C. reinhardtii* cell held stationary is measured experimentally via high-speed videography (figure 1a) and serves as input for numerical simulations. Physical parameters of the sample cell are given in table 1. We parameterize each flagellum by the arclength $s \in [0, L]$ along its centerline. From the measured waveform, we evaluate the velocities of the two flagella relative to the cell body, $U_i(s, t)$ for $i = 1, 2$, at each recorded time instant. The breaststroke beating

parameter	symbol	value
beating frequency	f_0	47 Hz
flagellum radius, length	r_0, L	0.125, 14 μm
anchored angle	ϕ	0.05π
semi-minor, semi-major axis	a, b	3.89, 5.95 μm

Table 1: Parameters of a representative *C. reinhardtii* cell measured in experiments. The value of flagellum radius is taken from Sager & Palade (1957).

of the two flagella is considered mirror-symmetric, and therefore the cell body undergoes only translational motion.

We simulate the dynamics of the model swimmer using a hybrid boundary element and regularized Stokeslet method (Smith 2009). The regularized Stokeslet is the exact solution to the Stokes equation subjected to a smoothed point force. With a specific smooth function, it can be expressed as (Cortez *et al.* 2005)

$$\mathbf{G}_\epsilon(\mathbf{x}_0, \mathbf{x}) = \frac{\mathbf{I}(R^2 + 2\epsilon^2) + \mathbf{R}\mathbf{R}}{R_\epsilon^3}, \quad (2.1)$$

where ϵ is the regularization parameter, $\mathbf{R} = \mathbf{x}_0 - \mathbf{x}$, and $R_\epsilon = \sqrt{R^2 + \epsilon^2}$.

We represent the motions of the cell body and the flagella by distributions of regularized Stokeslets on the body surface and along the flagellar centerlines, respectively. As verified by a test problem on a rigid scallop in Appendix A, this flagellar representation yields swimming dynamics that closely matches that obtained from the local slender body theory (Cox 1970) and shows only minor deviations from a nonlocal slender body theory (Johnson 1980). Denote the body surface by S and the flagella centerlines by C_i with $i = 1, 2$. The disturbance velocity in the fluid domain generated by the motion of the cell body is given by

$$\mathbf{u}_b(\mathbf{x}_0) = \frac{1}{8\pi\mu} \int_S \mathbf{G}_\epsilon(\mathbf{x}_0, \mathbf{x}) \cdot \mathbf{f}_b(\mathbf{x}) d\mathbf{x}, \quad (2.2)$$

and that by the flagella is given by

$$\mathbf{u}_i(\mathbf{x}_0) = \frac{1}{8\pi\mu} \int_{C_i} \mathbf{G}_\epsilon[\mathbf{x}_0, \mathbf{x}_i(s)] \cdot \mathbf{f}_i(s) ds, \quad \text{for } i = 1, 2, \quad (2.3)$$

where μ is the fluid viscosity, $\mathbf{x}_i(s)$ is the centerline position, and \mathbf{f}_b and \mathbf{f}_i are the hydrodynamic force densities exerted by the body and flagella on the fluid, respectively. When the evaluation points \mathbf{x}_0 lie on the boundaries, the total disturbance velocity due to the flagella and cell body satisfies the following constraints imposed by the no-slip condition,

$$\mathbf{u}_b(\mathbf{x}_0) + \sum_i \mathbf{u}_i(\mathbf{x}_0) = \mathbf{U}_b(t), \quad \text{for } \mathbf{x}_0 \in S, \quad (2.4)$$

$$\mathbf{u}_b(\mathbf{x}_0) + \sum_j \mathbf{u}_j(\mathbf{x}_0) = \mathbf{U}_b(t) + \mathbf{U}_i(s, t), \quad \text{for } \mathbf{x}_0 \in C_i \text{ and } i, j = 1, 2, \quad (2.5)$$

where $\mathbf{U}_b(t)$ is the instantaneous velocity of the cell body. Equations (2.4) and (2.5) incorporate both the interflagellar and the body-flagella HIs. Finally, the total hydrodynamic

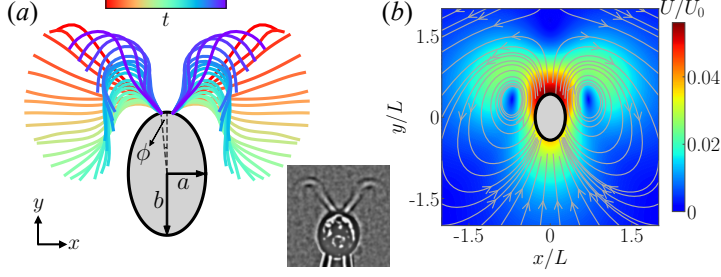


Figure 1: Model of swimming *C. reinhardtii*. (a) Flagellar waveform measured from experiments. Blue indicates recovery stroke, and red indicates power stroke. (b) Time-averaged disturbance flow field generated by the swimming model.

force and torque are zero,

$$\int_S \mathbf{f}_b(\mathbf{x}) d\mathbf{x} + \sum_i \int_{C_i} \mathbf{f}_i(s) ds = 0, \quad (2.6)$$

$$\int_S (\mathbf{x} - \mathbf{x}_b) \times \mathbf{f}_b(\mathbf{x}) d\mathbf{x} + \sum_i \int_{C_i} [\mathbf{x}_i(s) - \mathbf{x}_b] \times \mathbf{f}_i(s) ds = 0, \quad (2.7)$$

where the torques are evaluated relative to the body center \mathbf{x}_b .

We scale lengths by L , time by the beating period T , velocities by $U_0 = L/T$, and forces by $F_0 = \mu L^2/T$. The regularization parameter ϵ is taken to be the same as the flagellum radius r_0 (table 1). The integral formulations (2.2)–(2.7) are discretized into a system of linear equations for the unknowns \mathbf{U}_b , \mathbf{f}_b , and \mathbf{f}_i . Since the Stokeslet $\mathbf{G}_\epsilon(\mathbf{x}_0, \mathbf{x})$ often varies more rapidly near the source position \mathbf{x} than the hydrodynamic forces, the evaluation of the Stokeslet is performed on a finer grid than that of the forces (Smith 2009).

3. Results and discussion

3.1. Optimal cell body size for swimming

Figure 1(b) shows the disturbance velocity field of the model swimmer averaged over a beating period. There is one vortex on each side of the cell body, and a flow stagnation point exists in front of the swimmer along its swimming direction. These features closely resemble the measured flow field around free-swimming cells (Drescher *et al.* 2010). Using the parameters of the sample cell (table 1), we compute the time-averaged swimming speed $\langle U_b \rangle \approx 70.4 \mu\text{m/s}$, in agreement with the experimentally measured speed (Buchner *et al.* 2021). Slight variations in the anchored angle ϕ of the flagella (figure 1a) have little effect on the swimming performance.

We first evaluate the dependence of $\langle U_b \rangle$ on cell body size by varying the semi-major axis length b while using the same flagellar waveform data. As shown in figure 2(a), $\langle U_b \rangle$ varies non-monotonically with b/L , the ratio of body size to flagellar length. As the cell body becomes more slender (larger values of b/a), the maximum of $\langle U_b \rangle$ shifts to larger values of b/L . From a collection of about 40 cells, we measure an average $b/L = 0.38 \pm 0.08$, as indicated by the shaded regions in figure 2. For the sample cell ($b/a = 1.53$), the maximum occurs around $b/L \approx 0.21$, which is lower than its actual geometric ratio (0.425; see table 1) and lies more than one standard deviation below the measured average.

We further compute the swimming efficiency η using a definition similar to that in Lighthill

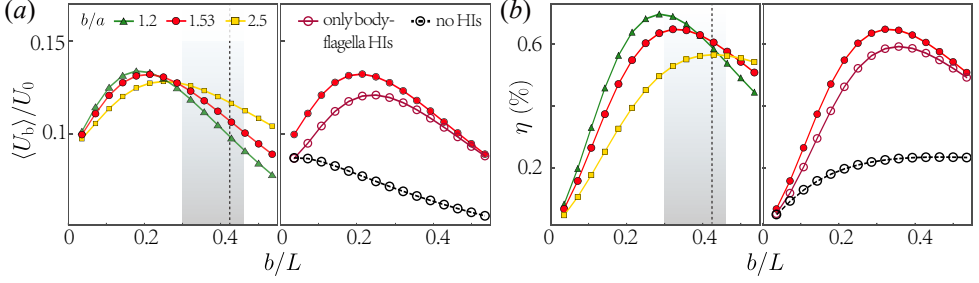


Figure 2: Effect of cell body size on swimming performance. (a) $\langle U_b \rangle / U_0$ as a function of b/L . (b) Swimming efficiency η as a function of b/L . The shaded areas indicate the distribution of b/L from experimental measurements. The vertical dashed lines mark the value of b/L of the sample cell. Other parameters are given in table 1.

(1952),

$$\eta = \frac{\zeta_b \langle U_b \rangle^2}{\left\langle \int_S \mathbf{f}_b \cdot \mathbf{U}_b \, d\mathbf{x} \right\rangle + \sum_i \left\langle \int_{C_i} \mathbf{f}_i \cdot (\mathbf{U}_b + \mathbf{U}_i) \, d\mathbf{s} \right\rangle}, \quad (3.1)$$

where ζ_b is the friction coefficient of a spheroid translating parallel to its long axis (Kim & Karrila 2013). Equation (3.1) expresses the ratio of the work required to drag a spheroid moving steadily at speed $\langle U_b \rangle$ to the work dissipated by the motions of the flagella and cell body. Figure 2(b) shows that η also exhibits a pronounced optimum with respect to b/L . Unlike $\langle U_b \rangle$, for the sample cell, the optimal value of b/L for η lies within one standard deviation of the measured average.

Removing the interflagellar HIs, which amounts to neglecting the disturbance velocity from the other flagellum in (2.5), has only a minor effect on the swimming performance (figures 2a and 2b, right panels). This is due to hydrodynamic screening by the cell body. Further removing the body-flagella HIs, i.e., neglecting \mathbf{u}_i in (2.4) and \mathbf{u}_b in (2.5), results in a much lower $\langle U_b \rangle$ and a monotonically decreasing trend with b . Therefore, the surprising increase of $\langle U_b \rangle$ at small values of b is attributed to increasingly strong body-flagella HIs as b increases. Meanwhile, the intrinsic viscous drag of the cell body $\zeta_b U_b$, also increases with b and eventually overwhelms the flagellar propulsion, leading to a decrease in $\langle U_b \rangle$ at sufficiently large b .

In figure 3, we compare the swimming speed $U_b(t)$ and the instantaneous displacement $y_b(t)$ of the cell body, obtained with and without body-flagella HIs. Our key observation is that body-flagella HIs not only increase the forward speed during the power stroke, but also reduce the backward speed during the recovery stroke (figure 3a); as a result, the swimmer achieves a larger forward displacement during the power stroke, and a smaller backward displacement during the recovery stroke (figure 3b). Over one period, the swimmer accumulates a net displacement of approximately $0.1 L$, about twice that achieved without body-flagella HIs.

3.2. Three-sphere model

To reveal the mechanisms underlying the enhancement of swimming performance by body-flagella HIs, we consider a three-sphere model consisting of a large central sphere of radius r_b , representing the cell body, and two smaller side spheres of radius r_f , representing the flagella (figure 4a). Unlike previous works (Friedrich & Jülicher 2012; Bennett & Golestanian 2013), we explicitly account for the no-slip boundary condition on the body surface by using the spherical image system \mathbf{G}_{im} (Kim & Karrila 2013). The two flagellar spheres, located at \mathbf{x}_i ($i = 1, 2$), are prescribed to move with velocity $v_0 \hat{\mathbf{t}}_i$ relative to the body and are mirror-

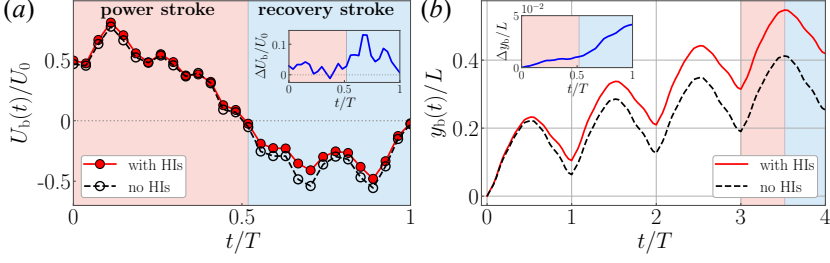


Figure 3: Effect of body-flagella HIs on (a) instantaneous swimming speed $U_b(t)$ and (b) instantaneous displacement $y_b(t)$. Inset shows the differences between the results obtained with and without body-flagella HIs for (a) $U_b(t)$ and (b) $y_b(t)$ over a beating period. Red and blue regions indicate power and recovery strokes, respectively.

symmetric with respect to the model centerline. Due to the force-free condition, the cell body, located at \mathbf{x}_b , develops an instantaneous translational velocity \mathbf{U}_b . The motion of the cell body induces a disturbance flow \mathbf{v}_b in the surrounding fluid,

$$\mathbf{v}_b(\mathbf{x}_0, \mathbf{x}_b; \mathbf{U}_b, r_b) = \frac{3}{4} r_b \mathbf{U}_b \cdot \left(1 + \frac{r_b^2}{6} \nabla^2 \right) \mathbf{G}(\mathbf{x}_0, \mathbf{x}_b), \quad (3.2)$$

where \mathbf{G} denotes the free-space Stokeslet.

The total drag force on the flagellar spheres is $\mathbf{F}_i = -6\pi\mu r_f(v_0 \hat{\mathbf{t}}_i + \mathbf{U}_b) + \mathbf{F}_{b \rightarrow i}$, where $\mathbf{F}_{b \rightarrow i}$ is the contribution to \mathbf{F}_i by the cell body, i.e., the body-to-flagella (B-to-F) force, given by

$$\mathbf{F}_{b \rightarrow i} = 6\pi\mu r_f \left[\mathbf{v}_b(\mathbf{x}_i, \mathbf{x}_b; \mathbf{U}_b, r_b) + \frac{1}{8\pi\mu} \mathbf{G}_{\text{im}}(\mathbf{x}_i, \mathbf{x}_b; r_b) \cdot \mathbf{F}_i \right]. \quad (3.3)$$

In (3.3), \mathbf{v}_b represents the dynamic component of the B-to-F force and exists only when the cell body is in motion. The term involving \mathbf{G}_{im} represents the static component of the B-to-F force and captures the effect of a nearby no-slip boundary on the flagellar force. The total drag force on the cell body is $\mathbf{F}_b = -6\pi\mu r_b \mathbf{U}_b + \sum_i \mathbf{F}_{i \rightarrow b}$, where $\mathbf{F}_{i \rightarrow b}$ is the contribution to the drag force acting on the cell body by the flagella-induced flow, i.e., the flagella-to-body (F-to-B) force. Using the strength of the image Stokeslet in \mathbf{G}_{im} , $\mathbf{F}_{i \rightarrow b}$ can be expressed as (Higdon 1979; Kim & Karrila 2013)

$$\mathbf{F}_{i \rightarrow b} = - \left[\left(\frac{3r_b}{2R_i} - \frac{r_b^3}{2R_i^3} \right) \hat{\mathbf{R}}_i \hat{\mathbf{R}}_i + \left(\frac{3r_b}{4R_i} + \frac{r_b^3}{4R_i^3} \right) (\mathbf{I} - \hat{\mathbf{R}}_i \hat{\mathbf{R}}_i) \right] \cdot \mathbf{F}_i, \quad (3.4)$$

where $\mathbf{R}_i = \mathbf{x}_i - \mathbf{x}_b$ and $\hat{\mathbf{R}}_i = \mathbf{R}_i/|\mathbf{R}_i|$. The body velocity \mathbf{U}_b can be obtained from the force-free condition: $\mathbf{F}_b + \sum_i \mathbf{F}_i = 0$.

3.3. Effective nonreciprocal interactions between cell body and flagella

The three-sphere model (§ 3.2) enables us to separately evaluate the effects of the F-to-B force and the dynamic and static components of the B-to-F force. We consider the time instant when the three spheres form an isosceles right triangle. The left flagellar sphere moves in the direction $\hat{\mathbf{t}}_1 = (\cos \alpha, \sin \alpha, 0)$, where we set the angle relative to the x axis $\alpha = 5\pi/4$. Reversing the direction of motion by setting $\alpha = \pi/4$ corresponds to switching from the power stroke to the recovery stroke and reverses the sign of U_b . Figure 4(b) shows that the F-to-B force alone can significantly reduce U_b compared with that without any HIs. This implies that the reduction in swimming speed during the recovery stroke (figure 3) results

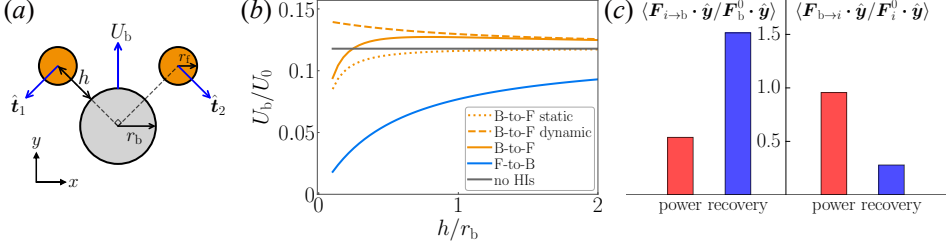


Figure 4: (a) Schematic of the three-sphere model. (b) Effect of different components of body-flagella HIs on the body speed U_b in the three-sphere model. The radius of the flagellar sphere $r_f = 0.1 r_b$. (c) Average of the normalized drag forces $\langle \mathbf{F}_{i \rightarrow b} \cdot \hat{\mathbf{y}} / \mathbf{F}_b^0 \cdot \hat{\mathbf{y}} \rangle$ and $\langle \mathbf{F}_{b \rightarrow i} \cdot \hat{\mathbf{y}} / \mathbf{F}_i^0 \cdot \hat{\mathbf{y}} \rangle$ (see text) over the power and recovery strokes.

from the impedance of the cell body by the flagella-induced flow. The dynamic component of the B-to-F force increases U_b , while the static component has the opposite effect but decays more rapidly with the distance from the body surface h . When $h \gtrsim r_b$, which is approximately the average separation between the flagella and cell body (figure 1a), the static component has a negligible effect on U_b . Therefore, the slight increase in U_b during the power stroke (figure 3a) may arise from the dominance of the dynamic component of the B-to-F force.

To verify the predictions from the three-sphere model, we evaluate how the cell body and flagella contribute to the drag forces on each other in the flagellated swimming model (§ 2). We approximate the spheroidal cell body as a sphere of radius $r_b = (a + b)/2$ and compute the F-to-B force $\mathbf{F}_{i \rightarrow b}(t)$ by integrating (3.4) along the arclength s , with \mathbf{F}_i replaced by the flagellar force density $\mathbf{f}_i(s)$. The dynamic component of the B-to-F force is computed as

$$\mathbf{F}_{b \rightarrow i}(t) = \int_{C_i} [\zeta_{\parallel} \mathbf{p}_i \mathbf{p}_i + \zeta_{\perp} (\mathbf{I} - \mathbf{p}_i \mathbf{p}_i)] \cdot \mathbf{v}_b[\mathbf{x}_i(s, t), \mathbf{x}_b; \mathbf{U}_b, r_b] ds, \quad (3.5)$$

where ζ_{\parallel} and ζ_{\perp} are the parallel and perpendicular drag coefficients of the slender flagella (Cox 1970), and \mathbf{p}_i is the unit tangent vector. To compare the relative strength of the effects of $\mathbf{F}_{i \rightarrow b}$ on the cell body and $\mathbf{F}_{b \rightarrow i}$ on the flagella, we normalize $\mathbf{F}_{i \rightarrow b}$ by $\mathbf{F}_b^0(t) = -6\pi\mu r_b \mathbf{U}_b(t)$, and $\mathbf{F}_{b \rightarrow i}$ by

$$\mathbf{F}_i^0(t) = - \int_{C_i} [\zeta_{\parallel} \mathbf{p}_i \mathbf{p}_i + \zeta_{\perp} (\mathbf{I} - \mathbf{p}_i \mathbf{p}_i)] \cdot [\mathbf{U}_b(t) + \mathbf{U}_i(s, t)] ds. \quad (3.6)$$

Here, \mathbf{F}_b^0 and \mathbf{F}_i^0 are the drag forces on the cell body and flagella, respectively, due to their own translational motions in a quiescent fluid. We normalize the components of $\mathbf{F}_{i \rightarrow b}$ and $\mathbf{F}_{b \rightarrow i}$ along the swimming direction $\hat{\mathbf{y}}$, and compute the average over the power and recovery strokes separately.

Figure 4(c) shows that the body-flagella HIs are effectively nonreciprocal during both the power and recovery strokes. During the power stroke, $\langle \mathbf{F}_{b \rightarrow i} \cdot \hat{\mathbf{y}} / \mathbf{F}_i^0 \cdot \hat{\mathbf{y}} \rangle$ is larger than $\langle \mathbf{F}_{i \rightarrow b} \cdot \hat{\mathbf{y}} / \mathbf{F}_b^0 \cdot \hat{\mathbf{y}} \rangle$, and the effect of the B-to-F force is stronger than that of F-to-B force, leading to a slightly larger forward speed (figure 3a). During the recovery stroke, $\langle \mathbf{F}_{i \rightarrow b} \cdot \hat{\mathbf{y}} / \mathbf{F}_b^0 \cdot \hat{\mathbf{y}} \rangle$ is larger than $\langle \mathbf{F}_{b \rightarrow i} \cdot \hat{\mathbf{y}} / \mathbf{F}_i^0 \cdot \hat{\mathbf{y}} \rangle$, and the effect of the F-to-B force dominates, leading to a smaller backward speed. The reversal of nonreciprocity when switching from the power stroke to the recovery stroke (figure 4c) arises from the time-nonreciprocal deformation of the flagella. During the power stroke, the flagella are extended straight and oriented perpendicular to the swimming direction, resulting in a stronger B-to-F effect. During the recovery stroke, the

flagella are coiled, more aligned with the swimming direction, and positioned closer to the cell body, resulting in a stronger F-to-B effect.

4. Conclusion

We modeled the swimming dynamics of *C. reinhardtii* using numerical simulations based on a boundary element method and experimentally measured flagellar waveform. We find that the swimming performance is significantly enhanced by the body-flagella HIs. As the cell body size increases, an optimal body size for swimming appears due to the competition between enhanced body-flagella HIs and increased viscous drag on the cell body. The measured average body size of *C. reinhardtii* is close to the computed optimal value that maximizes the swimming efficiency. Using the three-sphere model, we demonstrate that the body-flagella HIs are effectively nonreciprocal: the body affects the flagella more strongly than vice versa during the power stroke, while the reverse holds during the recovery stroke. As a result, the forward speed is larger than that without HIs during the power stroke, and the backward speed is smaller during the recovery stroke. Our results suggest a hydrodynamic interpretation for the characteristic body size of microalgae and may inform laboratory designs of biohybrid microrobots (Zhang *et al.* 2024).

Nonreciprocity generally emerges in interactions mediated by velocity fields. Another example of nonreciprocal HIs is found in dense cilia arrays (Hickey *et al.* 2023). Two other geometric features of eukaryotic microorganisms, namely the ratio of flagellar wave amplitude to wavelength and the body aspect ratio, also align with hydrodynamic predictions (Lisicki *et al.* 2024). Finally, beyond hydrodynamic effects, various factors can shape cell morphology. In particular, biological constraints naturally impose a lower limit on body size, as essential organelles like the nucleus and chloroplasts require a minimum volume to function.

Acknowledgements. We thank Jun Zhang for helpful conversations.

Funding. S.H. acknowledges support by the Fundamental Research Funds for the Central Universities. D.W. acknowledges support by National Natural Science Foundation of China (NSFC Grant No. 12204525). Z.L. acknowledges support by NSFC (Grant No. 12202438).

Declaration of interests. The authors report no conflict of interest.

Author ORCIDs. X. Hu, <https://orcid.org/0009-0002-2474-1287>; Z. Liu, <https://orcid.org/0000-0002-3158-3902>; D. Wei, <https://orcid.org/0000-0002-6226-0639>; S. Hu, <https://orcid.org/0000-0002-8415-4263>

Appendix A.

As a test problem for our implementation of the boundary element method, we consider a rigid scallop consisting of two slender rigid filaments hinged at a common end. This model does not swim on average but oscillates. The orientation of the upper filament is prescribed as $\theta(t) = \theta_0[\sin(\omega t) + 1]$, where θ_0 is the amplitude and ω is the frequency. The lower filament is held mirror-symmetric. We neglect the HIs between the two filaments.

From a nonlocal slender body theory (Johnson 1980), the filament velocity $\partial \mathbf{r} / \partial t$ is related to the force density \mathbf{f} through

$$8\pi\mu \frac{\partial \mathbf{r}(s, t)}{\partial t} = [c(\mathbf{I} + \mathbf{p}\mathbf{p}) + 2(\mathbf{I} - \mathbf{p}\mathbf{p})] \cdot \mathbf{f}(s) + \mathbf{K}[\mathbf{f}](s), \quad (\text{A } 1)$$

where $\mathbf{r}(s, t)$ is the centerline position, the slenderness parameter $c = |\ln(\epsilon^2 e)|$, the unit tangent vector $\mathbf{p} = (\cos \theta, \sin \theta)$, and the integral operator \mathbf{K} captures the nonlocal effects within the filament. The filament velocity can be decoupled into a translation of the hinged point with velocity $U(t)\hat{\mathbf{x}}$ and a rotation with angular velocity $\dot{\theta}$.

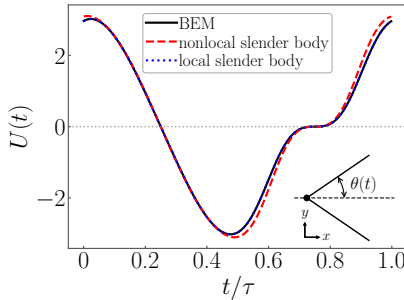


Figure 5: Comparison of the numerical results for a rigid scallop model, obtained from BEM, the local slender body theory, and a nonlocal slender body theory.

We discretize the filament centerline using Chebyshev points. The operator $\mathbf{K}[\mathbf{f}](s)$ is first regularized (Tornberg & Shelley 2004) and then evaluated via Clenshaw–Curtis quadrature with spectral accuracy (Trefethen 2000). Equation (A 1) forms a dense linear system for the unknowns \mathbf{f} and $U(t)$. By neglecting $\mathbf{K}[\mathbf{f}]$, (A 1) reduces to the local slender body theory (Cox 1970). Figure 5 shows that the result obtained from the BEM calculation using a line distribution of regularized Stokeslets agrees closely with the local slender theory and exhibits only minor deviations from the nonlocal slender body theory.

REFERENCES

- BENNETT, RACHEL R. & GOLESTANIAN, RAMIN 2013 Emergent run-and-tumble behavior in a simple model of chlamydomonas with intrinsic noise. *Phys. Rev. Lett.* **110**, 148102.
- BUCHNER, ABEL-JOHN, MULLER, KOEN, MEHMOOD, JUNAID & TAM, DANIEL 2021 Hopping trajectories due to long-range interactions determine surface accumulation of microalgae. *Proc. Natl. Acad. Sci. U.S.A.* **118** (20), e2102095118.
- CORTESE, DARIO & WAN, KIRSTY Y. 2021 Control of helical navigation by three-dimensional flagellar beating. *Phys. Rev. Lett.* **126**, 088003.
- CORTEZ, RICARDO, FAUCI, LISA & MEDOVNIKOV, ALEXEI 2005 The method of regularized stokeslets in three dimensions: Analysis, validation, and application to helical swimming. *Phys. Fluids* **17** (3), 031504.
- COX, RAYMOND G 1970 The motion of long slender bodies in a viscous fluid part 1. general theory. *J. Fluid Mech.* **44** (4), 791–810.
- DIAZ, KELIMAR, ROBINSON, TOMMIE L, AYDIN, YASEMIN OZKAN, AYDIN, ENES, GOLDMAN, DANIEL I & WAN, KIRSTY Y 2021 A minimal robophysical model of quadriflagellate self-propulsion. *Bioinspir. Biomim.* **16** (6), 066001.
- DRESCHER, KNUT, GOLDSTEIN, RAYMOND E, MICHEL, NICOLAS, POLIN, MARCO & TUVAL, IDAN 2010 Direct measurement of the flow field around swimming microorganisms. *Phys. Rev. Lett.* **105** (16), 168101.
- ELFASI, ROEI, ELIMELECH, YOSSEF & GAT, AMIR D 2018 Propulsion and maneuvering of an artificial microswimmer by two closely spaced waving elastic filaments. *Phys. Rev. Fluids* **3** (4), 044203.
- FRIEDRICH, BENJAMIN M. & JÜLICHER, FRANK 2012 Flagellar synchronization independent of hydrodynamic interactions. *Phys. Rev. Lett.* **109**, 138102.
- GILPIN, WILLIAM, BULL, MATTHEW STORM & PRAKASH, MANU 2020 The multiscale physics of cilia and flagella. *Nat. Rev. Phys.* **2** (2), 74–88.
- GOLDSTEIN, RAYMOND E. 2015 Green algae as model organisms for biological fluid dynamics. *Annu. Rev. Fluid Mech.* **47** (Volume 47, 2015), 343–375.
- HICKEY, DAVID J, GOLESTANIAN, RAMIN & VILFAN, ANDREJ 2023 Nonreciprocal interactions give rise to fast cilium synchronization in finite systems. *Proc. Natl. Acad. Sci. U.S.A.* **120** (40), e2307279120.
- HIGDON, JONATHAN JL 1979 A hydrodynamic analysis of flagellar propulsion. *J. Fluid Mech.* **90** (4), 685–711.
- HU, SHIYUAN & MENG, FANLONG 2024 Multiflagellate swimming controlled by hydrodynamic interactions. *Phys. Rev. Lett.* **132**, 204002.

- HU, SHIYUAN, ZHANG, JUN & SHELLEY, MICHAEL J 2022 Enhanced clamshell swimming with asymmetric beating at low reynolds number. *Soft Matter* **18** (18), 3605–3612.
- JOHNSON, ROBERT E 1980 An improved slender-body theory for stokes flow. *J. Fluid Mech.* **99** (2), 411–431.
- KIM, SANGTAE & KARRILA, SEPPO J 2013 *Microhydrodynamics: principles and selected applications*. Courier Corporation.
- LAUGA, ERIC 2007 Floppy swimming: Viscous locomotion of actuated elastica. *Phys. Rev. E* **75** (4), 041916.
- LEPTOS, KYRIACOS C, CHIOCCIOLI, MAURIZIO, FURLAN, SILVANO, PESCI, ADRIANA I & GOLDSTEIN, RAYMOND E 2023 Phototaxis of chlamydomonas arises from a tuned adaptive photoresponse shared with multicellular volvocine green algae. *Phys. Rev. E* **107** (1), 014404.
- LIGHTHILL, MICHAEL J 1952 On the squirming motion of nearly spherical deformable bodies through liquids at very small reynolds numbers. *Commun. Pure Appl. Math.* **5** (2), 109–118.
- LISICKI, MACIEJ, RODRIGUES, MARCOS F VELHO & LAUGA, ERIC 2024 Eukaryotic swimming cells are shaped by hydrodynamic constraints. *J. Fluid Mech.* **978**, R1.
- LIU, ZHAORONG, QIN, FENGHUA, ZHU, LAILAI, YANG, RUNHUAI & LUO, XISHENG 2020 Effects of the intrinsic curvature of elastic filaments on the propulsion of a flagellated microrobot. *Phys. Fluids* **32** (4), 041902.
- MACHIN, KE 1958 Wave propagation along flagella. *J. Exp. Biol.* **35** (4), 796–806.
- MOREAU, CLÉMENT, WALKER, BENJAMIN J., POON, REBECCA N., SOTO, DANIEL, GOLDMAN, DANIEL I., GAFFNEY, EAMONN A. & WAN, KIRSTY Y. 2024 Minimal design of a synthetic cilium. *Phys. Rev. Res.* **6**, L042061.
- PENG, Z., ELFRING, G. J. & PAK, O. S. 2017 Maximizing propulsive thrust of a driven filament at low Reynolds number via variable flexibility. *Soft Matter* **13** (12), 2339–2347.
- QUARANTA, GRETA, AUBIN-TAM, MARIE-EVE & TAM, DANIEL 2015 Hydrodynamics versus intracellular coupling in the synchronization of eukaryotic flagella. *Phys. Rev. Lett.* **115** (23), 238101.
- SAGER, RUTH & PALADE, GEORGE E 1957 Structure and development of the chloroplast in chlamydomonas i. the normal green cell. *J. Biophys. Biochem. Cytol.* **3** (3), 463–488.
- SARTORI, PABLO, GEYER, VEIKKO F, SCHOLICH, ANDRE, JÜLICHER, FRANK & HOWARD, JONATHAN 2016 Dynamic curvature regulation accounts for the symmetric and asymmetric beats of chlamydomonas flagella. *Elife* **5**, e13258.
- SMITH, DAVID J 2009 A boundary element regularized stokeslet method applied to cilia-and flagella-driven flow. *Proc. R. Soc. A: Math. Phys. Eng. Sci.* **465** (2112), 3605–3626.
- TAM, DANIEL & HOSOI, AE 2011 Optimal feeding and swimming gaits of biflagellated organisms. *Proc. Natl. Acad. Sci. U.S.A.* **108** (3), 1001–1006.
- TORNBERG, ANNA-KARIN & SHELLEY, MICHAEL J 2004 Simulating the dynamics and interactions of flexible fibers in stokes flows. *J. Comput. Phys.* **196** (1), 8–40.
- TREFETHEN, LLOYD N 2000 *Spectral methods in MATLAB*. SIAM.
- WEI, DA, DEHNAVI, PARVIZ GHODDOOSI, AUBIN-TAM, MARIE-EVE & TAM, DANIEL 2019 Is the zero reynolds number approximation valid for ciliary flows? *Physical Review Letters* **122** (12), 124502.
- WEI, DA, DEHNAVI, PARVIZ G., AUBIN-TAM, MARIE-EVE & TAM, DANIEL 2021 Measurements of the unsteady flow field around beating cilia. *Journal of Fluid Mechanics* **915**, A70.
- WIGGINS, CHRIS H & GOLDSTEIN, RAYMOND E 1998 Flexive and propulsive dynamics of elastica at low reynolds number. *Phys. Rev. Lett.* **80** (17), 3879.
- ZHANG, FANGYU, LI, ZHENGXING, CHEN, CHUANRUI, LUAN, HAO, FANG, RONNIE H, ZHANG, LIANGFANG & WANG, JOSEPH 2024 Biohybrid microalgae robots: design, fabrication, materials, and applications. *Adv. Mater.* **36** (3), 2303714.